Article

Enhanced Photoresponse and Wavelength Selectivity by SILAR-Coated Quantum Dots on Two-Dimensional WSe$_2$ Crystals

Soheil Ghods, Ali Esfandiar, Azam Iraji zad,* and Sajjad Vardast
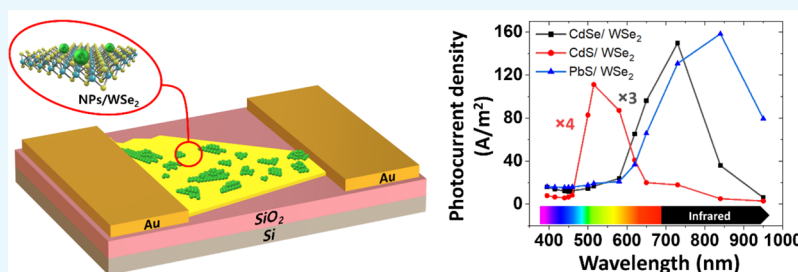
Read Online

ACCESS | 📊 Metrics & More | 📖 Article Recommendations | Ⓢ Supporting Information

ABSTRACT: High-performance photodetectors play crucial roles as an essential tool in many fields of science and technology, such as photonics, imaging, spectroscopy, and data communications. Demands for desired efficiency and low-cost new photodetectors through facile manufacturing methods have become a long-standing challenge. We used a simple successive ionic layer adsorption and reaction (SILAR) method to synthesize CdS, CdSe, and PbS nanoparticles directly grown on WSe$_2$ crystalline flakes. In addition to the excellent wavelength selectivity for (30 nm) CdS, (30 nm) CdSe, and (6 nm) PbS/WSe$_2$ heterostructures, the hybrid devices presented an efficient photodetector with a photoresponsivity of 48.72 A/W, a quantum efficiency of 71%, and a response time of 2.5−3.5 ms. Considering the energy band bending structure and numerical simulation data, the electric field distribution at interfaces and photocarrier generation/recombination rates have been studied. The introduced fabrication strategy is fully compatible with the semiconductor industry process, and it can be used as a novel method for fabricating wavelength-tunable and high-performance photodetectors toward innovative optoelectronic applications.

INTRODUCTION

Photodetector devices convert light irradiance to electrical signals, and as a vital optoelectronic elements have a wide range of applications in optical imaging,[1] communication,[2] remote sensing,[3] and environmental monitoring.[4] Common and core materials such as silicon,[5] germanium,[6] and GaAs[7] are the primary materials that are used for the fabrication of commercial photodetectors. Apart from the bulk nature of these materials, operating in a wide wavelength range is one of the drawbacks because the maximum photoresponse cannot be tuned at the desired wavelength for specific applications.[8]

Transition-metal dichalcogenides (TMDs) are emergent materials for photodetection that are broadly studied due to their capability of energy band gap engineering, layered structure, and chemical and physical doping possibilities.[9] Tungsten diselenide (WSe$_2$) is one of the TMDs that is less explored compared to its counterparts, such as WS$_2$ and MoS$_2$. The WSe$_2$ flakes have unique properties such as high carrier mobility (250 cm^2/V s),[10] strong optical absorption (2.13 cm^{-1}),[11] large luminescence intensity,[12] and high photoconversion efficiency[13] that make them a potent choice among 2D materials for electronic and optoelectronic applications. WSe$_2$ has a band gap in the range of ∼1.3 eV (as bulk form) to ∼1.8 eV (monolayer) that causes excellent absorption to the

visible and near-infrared (NIR) regions, rather than the UV region.[14] Stronger optical absorption can be achieved by fabricating heterostructures using TMDs and active semiconducting materials with designed energy band gap matching in which the responsivity can be enhanced by injecting more photocarriers and less recombination.[15,16]

It is known that most quantum dots as artificial atoms have tunable band gaps, strong optical absorption to a broad range of wavelengths from UV to IR, and high quantum efficiencies that make them interesting materials for heterostructure photodetectors.[17] For instance, CdS, CdSe, and PbS nanoparticles (NPs) are n-type semiconducting materials with band gaps in the range of ∼1.5 to ∼2.5 eV, which depends on the synthesis parameters.[18] They exhibit potential applications in the fields of photodetectors,[19] QLEDs,[20] solar cells,[21] and bioimaging.[22]
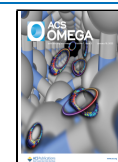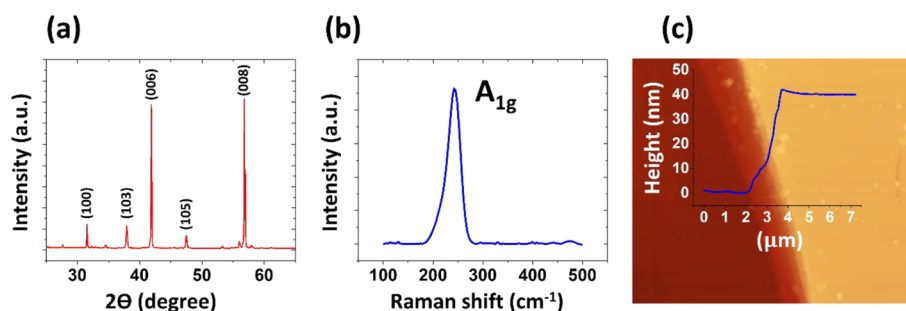
Figure 1. Characterization of the WSe_2 flake. (a) XRD pattern of the CVT-grown WSe_2 crystal. (b) Raman spectrum of the WSe_2 layer. (c) AFM image and the corresponding height profile from the edge of a typical flake.

Recently, low-dimension (0D/2D) hybrid photodetectors have attracted massive attention due to heterojunction formation between the NPs and the layered materials, which causes van der Waals contact at the interfaces.[23] This contact creates a built-in electric field in the junction that leads to an efficient photoinduced charge transport in the 2D nanoflake.[24] These heterostructures display unique properties such as high light absorption,[25] band tunability,[24] and scalability,[26] giving rise to a high potential for developing high-performance photodetectors and overcoming existing challenges.

Although there are many studies on 0D/2D photodetectors, there is still a necessity to build high-precision, adjustable, and affordable photodetectors using feasible approaches for commercialization.[27] To reduce the device preparation cost, synthesis methods of the materials are an important factor. One of the simple, inexpensive, highly efficient, and fast methods for synthesizing different semiconducting NPs is successive ionic layer adsorption and reaction (SILAR).[28]

In this study, we have presented a low-cost, accurate, and a rather simple method based on a novel NP/WSe_2 heterostructure on SiO_2/Si substrates by the SILAR method. The heterostructure formation between the WSe_2 flakes and the assembly of CdS, CdSe, and PbS NPs resulted in the enhanced absorption of light, responsivity, external quantum efficiency, and wavelength-tunable photodetectors. Moreover, using numerical simulation and scanning tunneling spectroscopy, the proposed mechanisms have been investigated.

■ RESULTS AND DISCUSSION

The X-ray diffraction (XRD) pattern of the grown material showed the crystalline phase of WSe_2 (Figure 1a). The diffraction peaks at 31.92°, 37.82°, 41.54°, 47.34°, and 56.42° are assigned to the (100), (103), (006), (105), and (008) crystal planes, respectively (38-1388, PDF 2 database). The confocal Raman spectrum (Figure 1b) from the transferred WSe_2 flake exhibits a peak centered at 247 cm^{-1} attributed to the A_{1g} mode of WSe_2.[31] The mean thickness of the used WSe_2 flakes was measured to be about 40 nm using an atomic force microscope (AFM) (Figure 1c). Step-like edges of the flake verify the layered structure of the chemical vapor transport (CVT)-grown crystal.

The schematic in Figure 2a shows the design of the device based on the WSe_2 flake and typical CdS NPs deposited using the SILAR method. The optical image of the WSe_2 flake is shown in Figure 2b, which is connected on both sides with Cr/Au electrodes. Figure 2c shows the field-emission scanning electron microscopy (FESEM) image of the edge of the WSe_2 flake before (the inset image in Figure 2c) and after CdS NP deposition. More detailed FESEM images indicate the
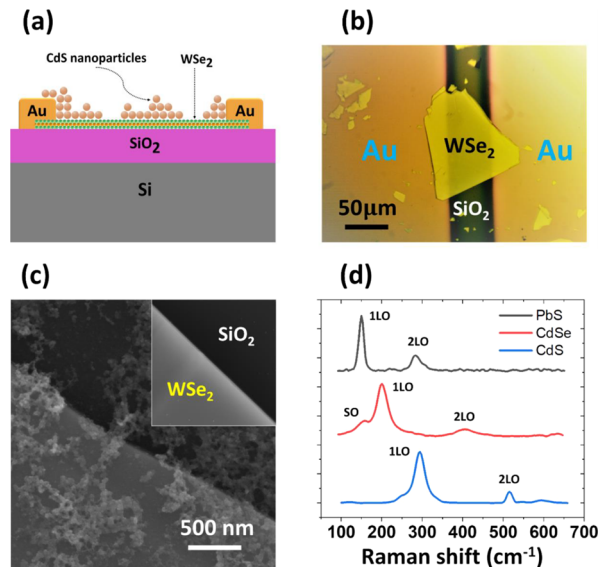

Figure 2. Characterization of NP/WSe_2. (a) Schematic illustration of the cross-sectional view of the CdS/WSe_2 NP device. (b) Optical image of the device based on the WSe_2 flake (before SILAR synthesis of the CdS NPs). (c) Scanning electron microscopy (SEM) image of the edge of the WSe_2 flake (before and after SILAR synthesis of CdS). (d) Raman spectrum of CdS, CdSe, and PbS NPs.

successful synthesis of scattered NPs on both surfaces of the WSe_2 flake and the SiO_2 substrate (Figures S3 and S4). Using the analysis performed by ImageJ software, the particle size is estimated to be between 40 ± 15 nm.

Figure 2d shows the Raman spectra of the CdS, CdSe, and PbS NPs, measured by a 532 nm laser excitation source at room temperature. For the CdS NPs coated on the WSe_2 sample, the spectrum exhibits intense peaks at 294 and 515 cm^{-1} that can be assigned to the longitudinal optical (LO) phonon mode and its overtone (2LO), respectively.[32] In the case of CdSe NPs coated on the WSe_2 sample, the peaks occur at 200 cm^{-1} (1LO) and 406 cm^{-1} (2LO).[33] In the PbS NP-coated sample, the spectrum exhibits peaks at 150 and 283 cm^{-1}, corresponding to the 1LO and 2LO phonon modes, respectively.[34]

Although deposition of the WSe_2 flake with NPs increases the absorption of light, which is an advantage for photodetectors, it can also increase the electrical resistance due to carrier scattering and prevent photons from interacting with the interface. For this reason, it is necessary to obtain an optimal condition for SILAR synthesis and deposition of the NPs on the WSe_2 flake in terms of thickness and morphology. Various parameters such as dip-coating time (T) and the

number of cycles (C) varied in five sample types (named as CdS(T-C)) have been investigated to obtain optimal conditions, where T is the dip-coating time in minutes (1.5, 2, 5, 10, and 20) and C presents the number of cycles (1, 3, 5, 10, and 20). For all samples, 0.05 M of the precursor concentration was utilized. At low T and C values, sparse decoration of the NPs was observed on the surface of WSe_2, while for SILAR deposition at high T and C conditions (e.g., CdS (10−10)), the substrate was almost entirely covered by NPs (Figure S4).

Figure 3a shows the photocurrent density results for bare WSe_2 and CdS NP-deposited samples using the SILAR
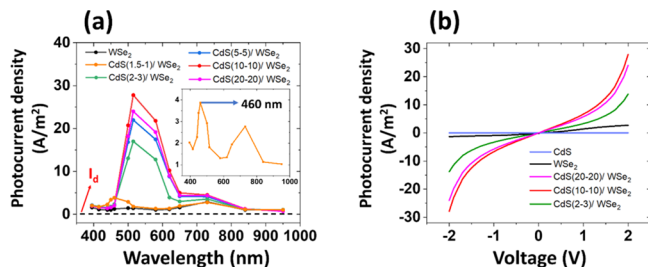

Figure 3. (a) Photocurrent density as a function of light-emitting diode (LED) irradiance at different wavelengths for the various conditions of SILAR synthesis. (b) Photocurrent density as a function of V_{sd} in the irradiated wavelengths that produce maximum photocurrent (a wavelength of 515 nm for CdS and CdS/WSe_2 and 730 nm for WSe_2 samples).

method. Under the irradiation of different wavelengths, all samples demonstrate a small photoresponse peak at 730 nm from WSe_2 and a significant peak at ∼520 nm corresponding to the CdS NPs (an average size of ∼30 nm and an energy band gap of 2.4 eV).[35] The photoresponse peak for the CdS (1.5−1)/WSe_2 sample shifts to 460 nm due to the smaller size of NPs. Since photocurrent for CdS (10−10)/WSe_2 and CdS (20−20)/WSe_2 samples is in the same order, the optimal condition for deposition of the CdS NPs on the WSe_2 flake was selected as 10 min of dip-coating time for 10 cycles. In Figure 3b, the photocurrent density is plotted as source-drain voltage (V_{sd}) versus the irradiated wavelengths that produce the maximum photocurrent. The photocurrent density is very low (<3 A/m^2) for the bare WSe_2 and CdS samples and increases significantly for the CdS/WSe_2 heterostructure device (the dark current for the CdS/WSe_2 structure is 0.16 A/m^2, shown in Figure 3a as a dotted line). It can be observed that the CdS (20−20)/WSe_2 sample presented less photocurrent in comparison with CdS (10−10)/WSe_2 because more NPs accumulating on the surface increases the electrical resistance of the sample (due to carrier scattering and covering/shadowing of the WSe_2 surface by NPs).

According to the optimal conditions of the SILAR process, we apply similar T (10 min) and C (10 cycles) on different precursor solutions with concentrations of 0.05 M for CdSe and 0.02 M for PbS NP deposition on WSe_2 flakes. In Figure 4a, the photocurrent density is plotted at different wavelengths for the three samples, namely, CdS/WSe_2, CdSe/WSe_2, and PbS/WSe_2. The maximum photocurrent values are observed at wavelengths of 520 nm (CdS/WSe_2), 730 nm (CdSe/WSe_2), and 840 nm (PbS/WSe_2). In Figure 4b, the photocurrent density is plotted as a function of V_{sd} for different samples at the irradiation wavelengths of the photocurrent peak. The hybrid structures ((CdS, CdSe, or PbS)/WSe_2) exhibited more
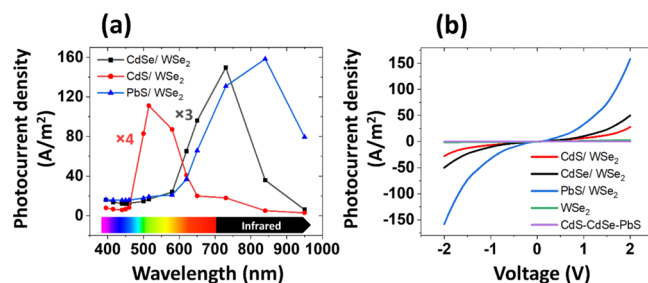

Figure 4. (a) Photocurrent as a function of wavelengths for CdS/WSe_2, CdSe/WSe_2, and PbS/WSe_2 samples. (b) Photocurrent density as a function of V_{sd} at the irradiated wavelengths that produce the maximum photocurrent (wavelength of 515 nm for CdS/WSe_2, 730 nm for CdSe/WSe_2, and 840 nm for PbS/WSe_2 samples).

than six times increase in photocurrent at V_{sd} of 2 V compared to the bare WSe_2, CdS, CdSe, and PbS structures, demonstrating the enhanced photoabsorption and synergic effect of the NPs on WSe_2 flakes to provide effective interfaces/junctions.

To study the energy band structures of the NP/WSe_2 interface, scanning tunneling spectroscopy (STS) was utilized as a powerful tool to estimate the band gap of materials. According to the STS results shown in Figure 5a, all the
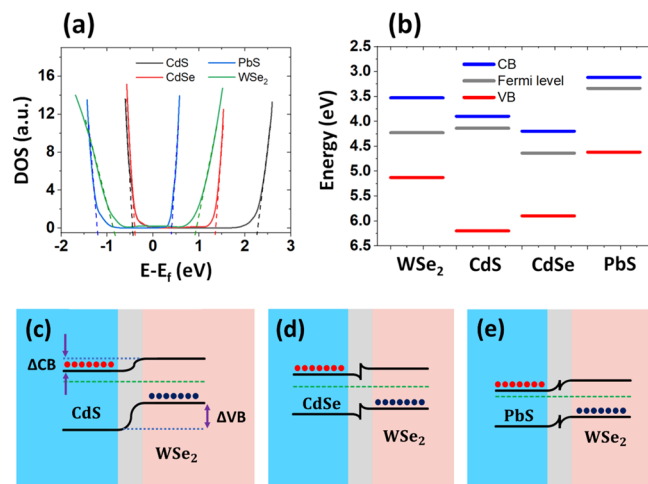

Figure 5. (a) STS spectra of the WSe_2 flake and CdS, CdSe, and PbS NPs on the Si substrate. The valence band and conduction band of each one are shown with dashed lines. (b) Band diagrams. (c) Energy band diagram at an unbiased mode for CdS/WSe_2, (d) CdSe/WSe_2, and (e) PbS/WSe_2.

materials represent an n-type behavior. For WSe_2, the band gap is 1.6 eV, and the electron affinity is 3.53 eV. Also, CdS, CdSe, and PbS showed band gaps (electron affinity) of 2.55 (3.9) eV, 1.7 (4.2) eV, and 1.5 (3.12) eV, respectively (Table 1).[36−38] Regarding these measured values from the STS analysis, their band structure diagrams are illustrated in Figure 5b.

According to the average particle sizes measured by the SEM images (Figures S3 and S4), the diameters were estimated to be ∼40 ± 15 nm for CdS and CdSe and ∼3 ± 1.5 nm for PbS. Since the purpose of this research was to fabricate photodetectors in different wavelength regions, SILAR synthesis for PbS was performed under the condition that the band gap of this material was located near the IR region. These results are

Table 1. Comparison of CdS-, CdSe-, and PbS-Measured Band Gaps with Reported Values for Different NP Sizes

structures	reported NP band gap in eV [NP size in nm]	measured band gap [eV], this work		references
		optical	STS	
CdS	2.4 [>6], 2.8 [3], 3.7 [2], 4.6 [1.2]	2.4 ± 0.2	2.55 ± 0.2	35−39
CdSe	1.8 [>5], 2.3 [3], 2.8 [2], 3.8 [0.8]	1.7 ± 0.2	1.7 ± 0.2	39
PbS	0.5 [>13], 0.75 [7], 0.9 [5], 1.4 [3], 2.3 [2]	1.5 ± 0.2	1.5 ± 0.2	40

in agreement with the previously reported energy band gap data (Table 1).

To understand the carrier injection and transport at interfaces under light irradiation, band alignments of the samples are demonstrated in Figure 5c−e. These diagrams show rather small ΔCB (the difference in the conduction band of the two connected materials shown in Figure 5c) as shown in Table 2, resulting in more electron transfer to WSe_2 than

Table 2. Comparison of ΔCB and ΔVB in CdS/WSe$_2$, CdSe/WSe$_2$, and PbS/WSe$_2$ Heterostructures

structures	ΔCB (eV)	ΔVB (eV)
CdS/WSe$_2$	0.37	1.13
CdSe/WSe$_2$	0.27	0.33
PbS/WSe$_2$	0.47	0.37

pristine materials. In the case of CdS/WSe$_2$, the ΔVB (the difference in the valence band of the two connected materials shown in Figure 5c) is higher than others (1.13 eV), which facilitates photocarrier (holes) transfer at the interface. In addition, band bending formation and the potential barrier (especially in CdSe/WSe$_2$ and PbS/WSe$_2$) at the interfaces hinder photoinduced electrons and holes from being recombined. Hence, the photocurrent in these structures increases significantly compared to the pristine WSe$_2$, CdS, CdSe, and PbS (Figure 4b).

To understand the nonlinear behavior of photocurrent and mechanism of charge carrier generation, the CdS/WSe$_2$ heterostructure was numerically simulated by technology computer-aided design (TCAD) software known as Silvaco Atlas. The ray tracing model was used to describe light propagation. The simulation of the optoelectronic device was divided into two specific models that are calculated concurrently at each DC bias point (transient time step):

1. Optical ray trace calculates the optical intensity at each grid point by using the real part of refractive index.

2. The absorption or photogeneration model uses the imaginary refractive index component to calculate a new carrier concentration at each grid point.

Figure 6a shows a schematic of the simulated structure. The dashed area indicates the WSe$_2$ and CdS interface, which is zoomed out in Figure 6b and used to represent the local electric field distribution. The relatively high electric field at the interface is due to the transfer of electrons from n^+(CdS) to n^-(WSe$_2$), as predicted by the STS analysis data (Figure 5b). It is known that in the presence of applied V_{sd}, photoinduced charge carriers drift into the electrodes and decrease their recombination rate. Therefore, more charge carriers can participate in the conductance, as observed in Figure 4b. The simulated total current density (electrons and holes) in the CdS/WSe$_2$ heterostructure is shown in Figure 7a, which is as high as 7.5 A/cm^2.

As shown in Figure 7a, moving away from the interface (in the $\mathbb{H}$ direction), the electric field and current density decrease. Since the carrier mobility in WSe$_2$ (145−173 cm^2/Vs) is higher than that of CdS (100 cm^2/Vs),[41,42] the total current density in the CdS layer is much lower than that in the WSe$_2$ region.

On the other hand, the high current density is due to the considerable impact generation rate, a three-particle production phenomenon, that is, high energy charge carriers in the built-in electric field experience scattering with bonded electrons in the valence band and excite them into the conduction band creating a new electron−hole pair. Due to the high energy of the secondary electron−hole pairs, an avalanche effect may be triggered.

Figure 7b shows the impact generation rate of the CdS/WSe$_2$ structure at V_{sd} = +2 V. The impact generation rate increases dramatically upon applying lateral voltage, where carriers gain enough energy for electron−hole production. However, the current density in the interface area is high (Figure 7a). Therefore, a high scattering rate results in a lower impact generation rate at the interface while it increases in both $\mathbb{H}$ directions.

Figure 7c,d show the recombination rate in the CdS/WSe$_2$ heterostructure for V_{sd} = 0 and V_{sd} = 2 V, respectively. The uniform rather high recombination rate at V_{sd} = 0 condition ($\mathbb{L}$ direction) indicates less chance for majority photoinduced charge carriers to be transferred to the contacts. By applying voltage in the $\mathbb{L}$ direction, tending carrier distribution to the left-hand side led to having less chance for recombination as is shown in the right side of Figure 7d[43] (22.3 cm^{-3} s^{-1} at V_{sd} = 0 V and 28 cm^{-3} s^{-1} at V_{sd} = 2 V).

To investigate the optical sensing properties of the samples, various parameters have been studied: photoresponsivity (R), EQE, NEP, D*, and photoconductivity gain (G) of the
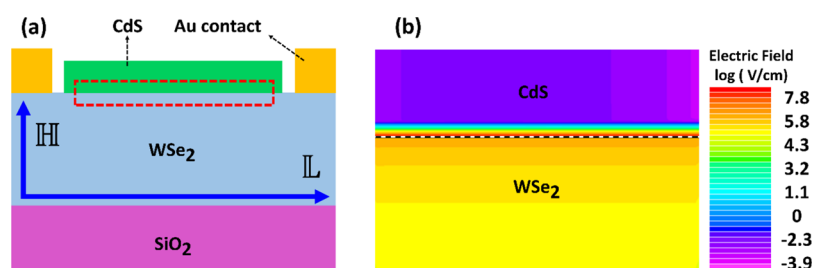

Figure 6. (a) Schematic of the CdS/WSe$_2$ structure ($\mathbb{H}$ and $\mathbb{L}$ represent two directions). (b) Simulated electric field of the dashed area in panel (a) in log scale and V_{sd} = +2 V.
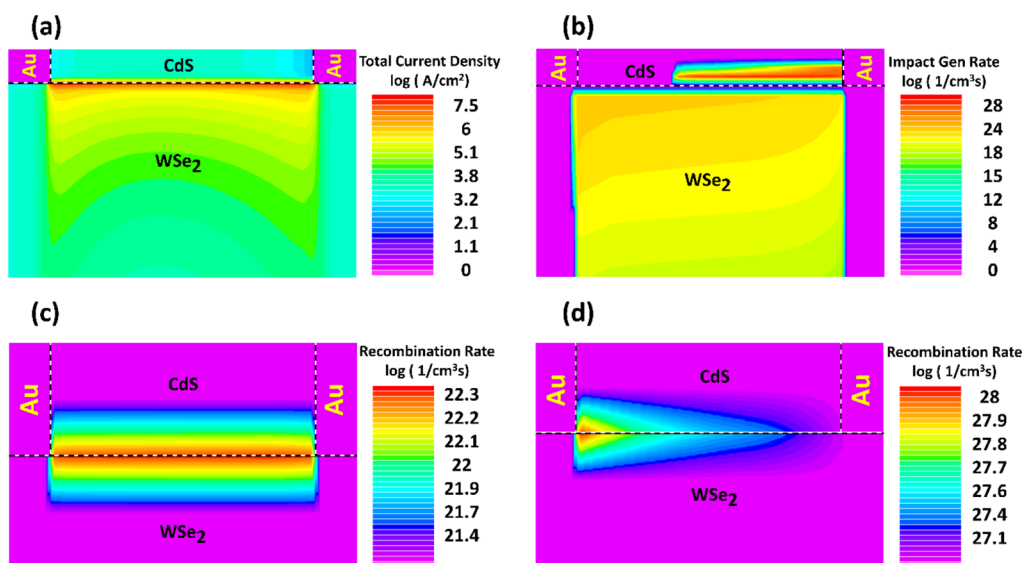
Figure 7. (a) Total current density in log scale for the CdS/WSe$_2$ structure and (b) impact generation rate in log scale for the CdS/WSe$_2$ structure at V_{sd} = +2 V. (c) Recombination rate in log scale for the CdS/WSe$_2$ structure at V_{sd} = 0 V and (d) V_{sd} = +2 V.

samples. Figure 8 shows the measured optoelectronic data under irradiation of LEDs at different wavelengths for (CdS, CdSe, and PbS)/WSe$_2$ devices.

The photoresponsivity (R) is defined as the ratio of photocurrent generated to the incident light power and can be calculated as:

$$R = (I - I_d)/P_{in} \qquad (1)$$

where I and I_d are the photocurrents under light illumination and dark mode, respectively, and P_{in} indicates the optical power density of the incident light. The photoresponsivity of the device is shown in Figure 8a, for the wavelengths ranging from 395 to 970 nm. The maximum responsivity of the samples was measured to be 8.78 A/W at 515 nm, 15.4 A/W at 735 nm, and 48.72 A/W at 850 nm for CdS/WSe$_2$, CdSe/WSe$_2$, and PbS/WSe$_2$, respectively.

The EQE parameter that is a ratio of the collected charge carriers (N_C) to the incident number of photons (N_I) is defined as:

$$EQE = (N_C/N_I) = (hcR/e\lambda) \qquad (2)$$

where h is the Planck constant, c indicates the speed of light, e is the electron charge, and λ is the wavelength of the incident light. Its direct relation to R keeps the peak positions in the same wavelengths as shown in Figure 8b. The EQE for PbS/WSe$_2$ is about 71%, which is a significant increase compared to bare WSe$_2$ (Figure S5), and for CdS/WSe$_2$ and CdSe/WSe$_2$, the EQE values are 21 and 26%, respectively.

As an essential parameter for a photodetector, the NEP parameter is evaluated which defines the required optical input power to achieve a signal-to-noise ratio (SNR) of one within a bandwidth of 1 Hz. The NEP is expressed as:

$$NEP = \frac{\sqrt{2eI_d}}{R} \qquad (3)$$

where R denotes responsivity and I_d is the dark current. The NEP values shown in Figure 8c for PbS/WSe$_2$ vary from 3.8×10^{-15} to 3.3×10^{-16}, while for other samples, the NEP values are in the range of 7.1×10^{-14} to 1.4×10^{-15}.
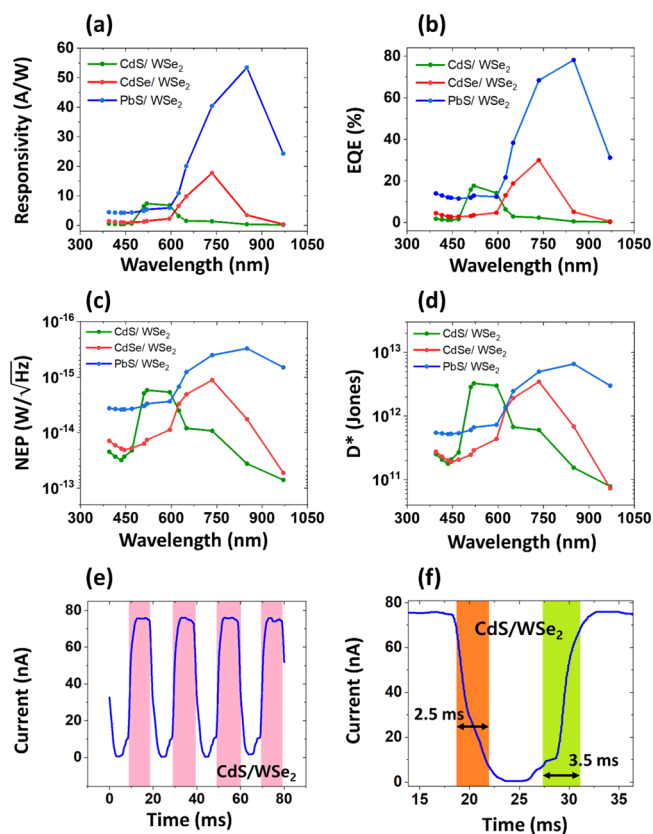
Figure 8. Photodetection parameters of the device. (a) Responsivity as a function of LED irradiance at different wavelengths. (b) External quantum efficiency (EQE) as a function of LED irradiance at different wavelengths. (c) Spectral dependence of the noise equivalent power (NEP) of the device. (d) Specific detectivity (D^*) of the device. (e) Response time of the CdS/WSe$_2$ device to a pulsed light (515 nm) source (the turn on and turn off times are the same, at 10 ms.) (f) Rising and falling times of the CdS/WSe$_2$ device to a pulsed light (515 nm) source (the turn on and turn off times are the same, at 10 ms).

Table 3. Comparison of Photodetector Parameters and Fabrication Methods of NP/WSe$_2$ with Similar Reported Devices

structures	wavelength (nm)	responsivity (A/W)	response time (s)	fabrication method	ref
WSe$_2$ (25 layers)	405−980	6.5×10^{-3}	6.5 ms	exfoliation	44
MoS$_2$/rGO NPs (monolayer)[a]	visible	2.1	18 ms	CVD/transferring	45
MoS$_2$/MoTe$_2$ (eight layers)	visible	0.62	10 μs	exfoliation/transferring	46
CdS nanowire	visible	360	10 ms	CVD	47
CdS/CdSO$_4$	400−600	0.3	14.4 ms	chemical methods	48
Sm:CdS	visible	0.2	120 ms	spraying	49
CdSSe nanobelt (60 layers)	550−650	10.4	4.7 ms	CVD	50
Sn^{2+}:PbS	660−980	15	$\sim$ 30 μs	chemical bath deposition	51
CdS/WSe$_2$ (50 layers)	450−650	8.8	2.5 ms	exfoliation/SILAR	this work
CdSe/WSe$_2$ (50 layers)	600−850	15.4	2.5 ms	exfoliation/SILAR	this work
PbS/WSe$_2$ (50 layers)	600−950	48.7	2.5 ms	exfoliation/SILAR	this work

[a]rGO: reduced graphene oxide.

The sensitivity of photodetectors relies on parameters such as bandwidth, the geometry of the structure, and the detector's active area and can be expressed as D^*. This parameter is calculated as:

$$D^* = \sqrt{A} / \text{NEP} \tag{4}$$

where A is the active area of the photodetector. Figure 8d shows the detectivity of the structures. Detectivity of CdS/WSe$_2$ and CdSe/WSe$_2$ varies from 7.8×10^{10} to 4.0×10^{12} Jones, and for PbS/WSe$_2$, it is in the range of 5.2×10^{11} to 6.1×10^{12} Jones.

The photoconductivity gain (G) that indicates the ratio of the detected charge carriers per single incident photon is represented as:

$$G = \tau_{\text{life}} / \tau_{\text{transit}} \tag{5}$$

In this relation, τ_{transit} is defined as $\tau_{\text{transit}} = L^2/\mu V_{\text{sd}}$, where L is the length of the channel and μ is the carrier mobility. The τ_{life} is approximated by the falling time of the transient I_{ph} during the on/off cycles of illumination. Since, for all structures, the channel length, mobility, and V_{sd} are approximately similar together, therefore, the difference in gain can be assigned to their τ_{life} (which is measured by the falling time). The measured photoconductivity gains of CdS/WSe$_2$, CdSe/WSe$_2$, and PbS/WSe$_2$ are 1.27×10^5, 6.25×10^4, and 1×10^5, respectively.

Figure 8e shows the typical response of CdS/WSe$_2$ to the pulsed light (515 and 10 ms duration). The calculated rising and falling times are 2.5 ms and 3.5 ms, respectively (Figure 8f). The rising (falling) time is defined as the time interval from 10% (90%) to 90% (10%) of the maximum (minimum) value, which is presented by green (orange) color. The long-term stability diagram, which shows the stability of the photodetector over time, is also shown in Figure S6. The response time diagram for CdSe/WSe$_2$ and PbS/WSe$_2$ photodetectors is shown in Figure S7.

Table 3 shows the comparison of the photodetector parameters (selectivity, responsivity, and response time) and fabrication methods presented in this research with other similar reported devices.

Wavelength selectivity is one of the most important challenging and vital parameters in photodetectors, and our sample shows better selectivity compared to other reported devices. Photodetectors based on TMDs and their heterostructure[44−46] have lower responsivity in the visible region compared to the samples of the current study. Although those photodetectors based on CdS obtained through a more complicated fabrication procedure presented higher photoresponsivity, the response time is still higher than our introduced SILAR-coated devices. Hence, the simple SILAR method, a rather high responsivity, and low response time in our samples make them as promising candidates for the photodetector industry.

CONCLUSIONS

In summary, we fabricated photodetectors based on NP (CdS, CdSe, and PbS)/WSe$_2$ heterostructures to improve the selectivity, responsivity, and response time compared with those made of WSe$_2$ and NPs. NPs create a built-in field resulting in a higher impact generation rate, good photoresponsivity (48.72 A/W), high EQE (71%), and an appropriate response time (2.5−3.5 ms). In addition, high selectivity (for wavelengths of 520, 735, and 850 nm) was achieved. The introduced structure is an innovative approach to build high-selectivity photodetectors that can open new windows for low-cost, mass-produced photodetectors.

METHODS

The crystal growth of WSe$_2$ was performed using the CVT method as follows: tungsten and selenium precursors were placed in a vacuum seal ampoule with a stoichiometric ratio of 1:2. The ampoule with a dimension of 20 cm length was placed in a furnace at 850 °C for 2 weeks (Figure S1). The CVT-grown WSe$_2$ crystal was mechanically exfoliated into a few layers of flakes and was transferred onto SiO$_2$/Si substrates using scotch tape. Then, Cr/Au electrodes were deposited on both sides of different selected flakes by physical vapor deposition and using a shadow mask. To deposit NPs, the SILAR method was carried out as given in the following text

Deposition of CdS. Cd^{2+} ions are adsorbed on the surface from a methanolic 0.05 M solution of Cd (NO$_3$)$_2$ and a 0.05 M solution of Na$_2$S in methanol/water (50/50 v/v) utilized as a S^{2-} source. A single SILAR cycle for CdS deposition was used as successive cycles of 1 min dip-coating each for Cd^{2+} precursor and then S^{2-} solution. After each precursor bath, the sample was rinsed by the corresponding solvent to remove the chemical residuals from the surface and then dried with an N$_2$ gun.[29]

Deposition of CdSe. Cd (NO$_3$)$_2$ (0.05 M) in ethanol solution was used as the Cd^{2+} precursor, and a 0.03 M selenide solution was prepared by dissolving 0.33 g of SeO$_2$ and 0.45 g of NaBH$_4$ in 60 mL of ethanol under a N$_2$ atmosphere and used as the Se^{2-} precursor.

Deposition of PbS. $Pb(NO_3)_2$ (0.02 M) in ethanol/water (50/50 v/v) was used as the Pb^{2+} precursor, and a 0.02 M solution of Na_2S in ethanol/water (50/50 v/v) was employed as the S^{2-} precursor source.[30]

To explore the crystal structure of the CVT-grown WSe_2 flake, XRD patterns were measured using a PANalytical diffractometer (Cu Kα, λ = 0.15418 nm), operating at 40 kV and equipped with a copper Kα radiation source. The thickness of the WSe_2 flake and the morphology of NP/WSe_2 were investigated using an AFM (Park Scientific CP-Research, Veeco) and an FESEM (MIRA3, T-Scan), respectively. Raman scattering measurements (XploRA, confocal Raman microscope, Horiba) were carried out at room temperature using a 532 nm laser as the excitation source. Electrical characterization of the devices was recorded using a Keithley 6487 picoammeter voltage source instrument. In the UV-to-NIR region, 13 LEDs were employed to illuminate the samples by wavelengths of 395, 415, 435, 445, 470, 510, 520, 595, 625, 650, 735, 850, and 970 nm. To achieve similar power density for different wavelengths illuminated on the sample, we adjusted the output power of LED sources using an optical power meter. To evaluate the time response of the device, a pulsed light was used and the photodetector response was controlled using a GW Instek GDS-1052-U oscilloscope along with the current-to-voltage converter circuit.

◼ ASSOCIATED CONTENT

ⓈI Supporting Information

The Supporting Information is available free of charge at https://pubs.acs.org/doi/10.1021/acsomega.1c05591.

Crystal growth, optical power dependence, NP size analysis, responsivity and EQE of WSe_2 and PbS/WSe_2, long-term stability, pulsed light response, and EDS spectra of NPs (PDF)

◼ AUTHOR INFORMATION

Corresponding Author

Azam Iraji zad − *Department of Physics and Institute for Nanoscience and Nanotechnology, Sharif University of Technology, Tehran 11155-9161, Iran;* ⓞ orcid.org/0000-0001-6537-0991; Email: iraji@sharif.edu

Authors

Soheil Ghods − *Department of Physics, Sharif University of Technology, Tehran 11155-9161, Iran;* ⓞ orcid.org/0000-0002-4374-2579

Ali Esfandiar − *Department of Physics, Sharif University of Technology, Tehran 11155-9161, Iran;* ⓞ orcid.org/0000-0002-7566-9791

Sajjad Vardast − *Department of Electrical Engineering, Sharif University of Technology, Tehran 11155-9161, Iran*

Complete contact information is available at:
https://pubs.acs.org/10.1021/acsomega.1c05591

Notes

The authors declare no competing financial interest.

◼ REFERENCES

(1) Lien, M.-B.; Liu, C.-H.; Chun, I. Y.; Ravishankar, S.; Nien, H.; Zhou, M.; Fessler, J. A.; Zhong, Z.; Norris, T. B. Ranging and Light Field Imaging with Transparent Photodetectors. *Nat. Photonics* **2020**, *14*, 143−148.

(2) Lu, Y.; Wang, Y.; Xu, C.; Xie, C.; Li, W.; Ding, J.; Zhou, W.; Qin, Z.; Shen, X.; Luo, L. Construction Of Ptse$_2$/Ge Heterostructure-Based Short-Wavelength Infrared Photodetector Array For Image Sensing And Optical Communication Applications. *Nanoscale* **2021**, *13*, 7606−7612.

(3) Konstantatos, G. Current Status and Technological Prospect of Photodetectors Based on Two-Dimensional Materials. *Nat. Commun.* **2018**, *9*, 5266.

(4) Dong, T.; Simões, J.; Yang, Z. Flexible Photodetector Based on 2D Materials: Processing, Architectures, and Applications. *Adv. Mater. Interfaces* **2020**, *7*, No. 1901657.

(5) Liu, J.; Cristoloveanu, S.; Wan, J. *A Review On The Recent Progress Of Silicon-On-Insulator-Based Photodetectors. physica status solidi (a)*; 2021; Vol. 218, pp 2000751.

(6) Cui, J.; Li, T.; Yang, F.; Cui, W.; Chen, H. The Dual-Injection Ge-On-Si Photodetectors with High Saturation Power By Optimizing Light Field Distribution. *Opt. Commun.* **2021**, *480*, No. 126467.

(7) Wang, D.; Chen, X.; Fang, X.; Tang, J.; Lin, F.; Wang, X.; Liu, G.; Liao, L.; Ho, J.; Wei, Z. Photoresponse Improvement Of Mixed-Dimensional 1D−2D Gaas Photodetectors By Incorporating Constructive Interface States. *Nanoscale* **2021**, *13*, 1086−1092.

(8) Dardano, P.; Ferrara, M. A. Integrated Photodetectors Based on Group IV and Colloidal Semiconductors: Current State of Affairs. *Micromachines* **2020**, *11*, 842.

(9) Ghods, S.; Esfandiar, A. Plasmonic Enhancement of Photocurrent Generation in Two-Dimensional Heterostructure of WSe_2/MoS_2. *Nanotechnology* **2021**, *32*, 325203.

(10) Tiwari, P.; Patel, K.; Krishnia, L.; Kumari, R.; Tyagi, P. K. Potential Application of Multilayer N-Type Tungsten Diselenide (WSe_2) Sheet as Transparent Conducting Electrode in Silicon Heterojunction Solar Cell. *Comput. Mater. Sci.* **2017**, *136*, 102−108.

(11) Jung, G.-H.; Yoo, S.; Park, Q.-H. Measuring the Optical Permittivity of Two-Dimensional Materials without a Priori Knowledge of Electronic Transitions. *NANO* **2018**, *8*, 263−270.

(12) Tonndorf, P.; Schmidt, R.; Böttger, P.; Zhang, X.; Börner, J.; Liebig, A.; Albrecht, M.; Kloc, C.; Gordan, O.; Zahn, D. R. T.; Michaelis de Vasconcellos, S.; Bratschitsch, R. Photoluminescence Emission and Raman Response of Monolayer MoS_2, $MoSe_2$, and WSe_2. *Opt. Express* **2013**, *21*, 4908−4916.

(13) Durairasan, M.; Karthik, P. S.; Balaji, J.; Rajeshkanna, B. Design and Fabrication of WSe_2/CNTs Hybrid Network: A Highly Efficient and Stable Electrodes for Dye Sensitized Solar Cells (DSSCs). *Diamond Relat. Mater.* **2021**, *111*, No. 108174.

(14) Patel, R.; Pataniya, P.; Patel, M.; Sumesh, C. Wse$_2$ Crystals On Paper: Flexible, Large Area And Broadband Photodetectors. *Nanotechnology* **2021**, *32*, 505202.

(15) Wang, Z.; Altmann, P.; Gadermaier, C.; Yang, Y.; Li, W.; Ghirardini, L.; Trovatello, C.; Finazzi, M.; Duò, L.; Celebrano, M.; et al. Phonon-Mediated Interlayer Charge Separation And Recombination In A Mose$_2$/Wse$_2$ Heterostructure. *Nano Lett.* **2021**, *21*, 2165−2173.

(16) Rao, G.; Wang, X.; Wang, Y.; Wangyang, P.; Yan, C.; Chu, J.; Xue, L.; Gong, C.; Huang, J.; Xiong, J.; Li, Y. Two-dimensional Heterostructure Promoted Infrared Photodetection Devices. *InfoMat* **2019**, *1*, 272−288.

(17) Khan, I.; Saeed, K.; Khan, I. Nanoparticles: Properties, Applications and Toxicities. *Arab. J. Chem.* **2019**, *12*, 908−931.

(18) Matiur, R.; Abuelwafa, A.; Putri, A.; Kato, S.; Kishi, N.; Soga, T. Annealing Effects On Structural And Photovoltaic Properties Of The Dip-SILAR-Prepared Bismuth Oxyhalides (Bioi, Bi7o9i3, Bi5o7i) Films. *SN Appl. Sci.* **2021**, *3*, 138.

(19) Shelke, N. T.; Karle, S. C.; Karche, B. R. Photoresponse Properties of CdSe Thin Film Photodetector. *J. Mater. Sci.: Mater. Electron.* **2020**, *31*, 15061−15069.

(20) Yuan, Q.; Wang, T.; Yu, P.; Zhang, H.; Zhang, H.; Ji, W. A Review on the Electroluminescence Properties of Quantum-Dot Light-Emitting Diodes. *Org. Electron.* **2021**, *90*, No. 106086.

(21) Rahman, M. M.; Karim, M. R.; Alharbi, H. F.; Aldokhayel, B.; Uzzaman, T.; Zahir, H. Cadmium Selenide Quantum Dots for Solar Cell Applications: A Review. *Chem. − Asian J.* **2021**, *16*, 902−921.

(22) Pandey, S.; Bodas, D. High-Quality Quantum Dots for Multiplexed Bioimaging: A Critical Review. *Adv. Colloid Interface Sci.* **2020**, *278*, No. 102137.

(23) Selamneni, V.; Anand, P. P.; Singh, A.; Sahatiya, P. Hybrid 0D−2D WS$_2$-Qds (N)/Sns (P) As Distributed Heterojunctions For Highly Responsive Flexible Broad-Band Photodetectors. *ACS Appl. Electron. Mater.* **2021**, *3*, 4105−4114.

(24) Selamneni, V.; Ganeshan, S. K.; Sahatiya, P. All MoS$_2$ Based 2D/0D Localized Unipolar Heterojunctions as Flexible Broadband (UV-Vis-NIR) Photodetectors. *J. Mater. Chem. C Mater. Opt. Electron. Devices* **2020**, *8*, 11593−11602.

(25) Fang, J.; Zhou, Z.; Xiao, M.; Lou, Z.; Wei, Z.; Shen, G. Recent Advances in Low-dimensional Semiconductor Nanomaterials and Their Applications in High-performance Photodetectors. *InfoMat* **2020**, *2*, 291−317.

(26) Peng, M.; Wang, Y.; Shen, Q.; Xie, X.; Zheng, H.; Ma, W.; Wen, Z.; Sun, X. High-Performance Flexible and Broadband Photodetectors Based on PbS Quantum Dots/ZnO Nanoparticles Heterostructure. *Sci. China Mater.* **2019**, *62*, 225−235.

(27) Jariwala, D.; Marks, T. J.; Hersam, M. C. Mixed-Dimensional van Der Waals Heterostructures. *Nature Mater* **2017**, *16*, 170−181.

(28) Siabi-Garjan, A.; Farazin, J.; Pirgholi-Givi, G.; Azizian-Kalandaragh, Y. Formation Of Cds/ZnS Nanoparticles In Polymer Matrix By SILAR Method: Experiments And Exploring Its Optical Properties With DDA Calculations. *Optik* **2021**, *242*, No. 166958.

(29) Samadpour, M. Efficient CdS/CdSe/ZnS Quantum Dot Sensitized Solar Cells Prepared by ZnS Treatment from Methanol Solvent. *Sol. Energy* **2017**, *144*, 63−70.

(30) Samadpour, M.; Arabzade, S. Graphene/CuS/PbS Nanocomposite as an Effective Counter Electrode for Quantum Dot Sensitized Solar Cells. *J. Alloys Compd.* **2017**, *696*, 369−375.

(31) Rahul; Arora, S. Quantitative Evaluation Of Nonlinear Temperature Dependence Of Raman Shift In Exfoliated Wse$_2$ Nanosheets. *J. Electron. Mater.* **2021**, *50*, 7126−7132.

(32) Maity, P.; Kumar, S.; Kumar, R.; Jha, S.; Bhattacharyya, D.; Barman, S.; Chatterjee, S.; Pal, B.; Ghosh, A. Role Of Cobalt Doping In Cds Quantum Dots For Potential Application In Thin Film Optoelectronic Devices. *J. Phys. Chem. C* **2021**, *125*, 2074−2088.

(33) Bhand, G. R.; Chaure, N. B. Synthesis of CdTe, CdSe and CdTe/CdSe Core/Shell QDs from Wet Chemical Colloidal Method. *Mater. Sci. Semicond. Process.* **2017**, *68*, 279−287.

(34) Suganya, M.; Balu, A. R. PbS Nanopowder − Synthesis, Characterization and Antimicrobial Activity. *Mater. Sci.-Pol.* **2017**, *35*, 322−328.

(35) Guisbiers, G. Advances in Thermodynamic Modelling of Nanoparticles. *Adv. Phys.: X* **2019**, *4*, No. 1668299.

(36) Mishra, A.; Rana, C.; Saha, S. Fabrication And Comparison Of Heterojunction Solar Cells From CdS/PbS Nanoparticles And CdS/PbS Bulk. *Nano Express* **2020**, *1*, No. 020024.

(37) Babu, N.; Khadar, M. Composite Formation In CdSe:Cu$_2$Se Nanocrystal Films, Charge Transport Characteristics And Heterojunction Performance. *RSC Adv.* **2020**, *10*, 8842−8852.

(38) Ahmmed, S.; Aktar, A.; Rahman, M.; Hossain, J.; Ismail, A. A Numerical Simulation Of High Efficiency CdS/CdTe Based Solar Cell Using Nio HTL And Zno TCO. *Optik* **2020**, *223*, No. 165625.

(39) Baskoutas, S.; Terzis, A. F. Size-Dependent Band Gap of Colloidal Quantum Dots. *J. Appl. Phys.* **2006**, *99*, No. 013708.

(40) Vankhade, D.; Ray, J.; Chaudhuri, T. Nanocrystalline PbS Thin Films as Photodetectors. *Adv. Sci. Lett.* **2016**, *22*, 1022−1025.

(41) Fathi, M.; Abderrezek, M.; Djahli, F.; Ayad, M. Study of Thin Film Solar Cells in High Temperature Condition. *Energy Procedia* **2015**, *74*, 1410−1417.

(42) Kam, K.-K. *Electrical Properties of WSe2, WS2, MoSe2, MoS2, and Their Use as Photoanodes in a Semiconductor Liquid Junction Solar Cell*; Iowa State University, 2018.

(43) Taur, Y.; Ning, T. H. *Fundamentals of Modern VLSI Devices*; Cambridge University Press, 2013.

(44) Ma, Y.; Liu, D.; Hao, J.; Wang, L.; Wang, W. High-Performance Flexible Wse$_2$ Flake Photodetector With Broadband Detection Capability. *AIP Adv.* **2020**, *10*, 125027.

(45) Kumar, R.; Goel, N.; Raliya, R.; Biswas, P.; Kumar, M. High-Performance Photodetector Based On Hybrid Of Mos$_2$ And Reduced Graphene Oxide. *Nanotechnology* **2018**, *29*, 404001.

(46) Ahn, J.; Kang, J.; Kyhm, J.; Choi, H.; Kim, M.; Ahn, D.; Kim, D.; Ahn, I.; Park, J.; Park, S.; et al. Self-Powered Visible−Invisible Multiband Detection And Imaging Achieved Using High-Performance 2D MoTe$_2$/MoS$_2$ Semivertical Heterojunction Photodiodes. *ACS Appl. Mater. Interfaces* **2020**, *12*, 10858−10866.

(47) Gou, G.; Dai, G.; Qian, C.; Liu, Y.; Fu, Y.; Tian, Z.; He, Y.; Kong, L.; Yang, J.; Sun, J.; Gao, Y. High-Performance Ultraviolet Photodetectors Based on CdS/CdS:SnS$_2$ superlattice Nanowires. *Nanoscale* **2016**, *8*, 14580−14586.

(48) Li, Z.; Davar, F.; Chen, J.; Li, Z.; Fang, X. CdS/CdSO$_4$ Nanoflower-Based Photodetector With Enhanced Photoelectric Performances. *ACS Appl. Nano Mater.* **2020**, *3*, 10190−10199.

(49) Shkir, M.; Ashraf, I.; Khan, A.; Khan, M.; El-Toni, A.; AlFaify, S. A Facile Spray Pyrolysis Fabrication Of Sm:CdS Thin Films For High-Performance Photodetector Applications. *Sens. Actuators, A* **2020**, *306*, No. 111952.

(50) Li, X.; Tan, Q.; Feng, X.; Wang, Q.; Liu, Y. Wavelength-Controlled Photodetector Based on Single CdSSe Nanobelt. *Nanoscale Res. Lett.* **2018**, *13*, 171.

(51) Liu, S.; Fei, G.; Xu, S.; Gao, X. High-Performance Visible-Near IR Photodetectors Based On High-Quality Sn2+-Sensitized Pbs Films. *J. Alloys Compd.* **2021**, *883*, No. 160860.